LA-UR-99-3183

96339

pproved for public release;
distribution is unlimited

Title: **Neutrino Physics at Fermilab**

Author(s): Geoffrey B. Mills, Frederick Federspiel, Gerald Garvey, William C. Louis, Rex Tayloe, Vern Sandberg, Ben Sapp, D. Hywel White

P-25

Submitted to: DOE Office of Scientific and Technical Information (OSTI)

Los Alamos
NATIONAL LABORATORY

Form 836 (10/96)
ST 2629

DISCLAIMER

Neutrino Physics at Fermilab

Frederick Federspiel, Gerald Garvey, William C. Louis,
Geoffrey B. Mills*, Rex Tayloe, Vern Sandberg, Ben Sapp, D. Hywel White

P-25

Abstract

The Liquid Scintillator Neutrino Detector (LSND), located at the LANSCE (formerly LAMPF) linear accelerator at Los Alamos National Laboratory, has seen evidence for the oscillation of neutrinos, and hence neutrino mass. That discovery was the impetus for this LDRD project, begun in 1996. The goal of this project was to define the appropriate technologies to use in a follow up experiment and to set in place the requirements for such an experiment.

Background and Research Objectives

This LDRD research was motivated by two important pieces of evidence for neutrino oscillations. The first is the observation of events by the LSND collaboration that are consistent $\bar{\nu}_\mu \rightarrow \bar{\nu}_e$ and $\nu_\mu \rightarrow \nu_e$ oscillations. The second is the observed deficit of atmospheric neutrinos which may be attributed to disappearance through oscillations. In 1995 and 1996, the LSND experiment at Los Alamos reported evidence(Ref. 1) for $\bar{\nu}_\mu \rightarrow \bar{\nu}_e$ oscillations at the level of 0.3 percent transmutation probability. Since that time the signal has grown stronger as more data has been accumulated. Previous oscillation searches have not seen oscillations in the region allowed by LSND with $\Delta m^2 > 4$. This isolates the most favored region at low Δm^2. Since the original LSND publication, the KARMEN experiment at the ISIS facility and the LSND experiment have obtained further results that strengthen the case for a $\bar{\nu}_\mu \rightarrow \bar{\nu}_e$ oscillation signal. KARMEN(Ref. 2) observes an excess of events in their data taken through 1996 consistent with the LSND $\bar{\nu}_\mu \rightarrow \bar{\nu}_e$ oscillation signal, but only at the one standard deviation level due to low

*Principal Investigator, e-mail: mills@lanl.gov

luminosity and high rates of cosmic-ray background. Therefore, KARMEN prefers to quote an upper limit. LSND has released preliminary results from the 1996-1998 runs consistent with the previous LSND results. LSND (Ref. 3) also is able to search for $\nu_\mu \rightarrow \nu_e$ oscillations using π^+ that decay in flight. This decay-in-flight oscillation search has different backgrounds and systematics than the decay-at-rest search, and the results are consistent with the decay-at-rest signal.

The LSND result has had important effects on the understanding of neutrino masses. It hints at the possibility of neutrino masses in the range of 1 eV which have profound effects on the models of the early universe. Neutrinos with masses in the few electron volt range could determine whether the universe is closed or open. The result shows that at least one of the neutrinos must have a mass in the range of 0.5 eV or greater. It is crucial to measure the Δm^2 parameter of the oscillation and also the $\sin^2(2\theta)$ parameter accurately to make further progress in the area. The purpose of this LDRD project was to determine the best and most efficient way to accomplish this task. A verification of the LSND result in a setting with a better controlled measurement and with higher statistics and precision.

There are several questions which must be addressed when contemplating a new generation of experiment. It is clear that the experimental environment must be optimized for the Δm^2 range that LSND is sensitive to, taking into account constraints from other experiments. This range is 0.1 eV^2 to 10 eV^2 which has a direct bearing on the experimental design. The oscillation probability for the simple two generation oscillation picture is given by

$$P(\overline{\nu}_\mu \rightarrow \overline{\nu}_e) = \sin^2 2\theta \ \sin^2\left(\Delta m^2 \frac{L}{E_\nu}\right).$$

The experimentally important parameters are L, the distance from the neutrino source to the detection apparatus, and E_ν, the neutrino energy. In order to measure the oscillation parameter well, the product Δm^2 L/E should be roughly in the range 0.5-2, and thus for the LSND signal, this translates into a L/E of 0.2 meters/MeV to 5 meters/MeV. An experiment which is to follow up on the LSND must therefore have a neutrino beam energy and distance in this range with sufficient dynamic range in energy to see the oscillation effect.

A candidate scenario has emerged from this work. The Fermilab 8 GeV proton booster is an intense source of protons that might be used to produce neutrinos in an energy range of roughly 500-1000 MeV. If detector could be placed at 500 meters from the source, it might be sensitive to the LSND signal. The goal and objective of this R&D effort was to explore the technological requirements for such an enterprise.

Importance to LANL's Science and Technology Base and National R&D Needs

Los Alamos has a long tradition of excellence in the field of Neutrino Physics. Indeed, the first observations of neutrinos were made by Los Alamos physicists many years ago. In this spirit the LSND detector has now uncovered evidence that neutrinos may have a finite rest mass, carrying on a tradition of discovery at Los Alamos. This is a profound and revolutionary discovery if born out by further experiments. It is clear, however, that the LSND experiment has been pushed to its limits in terms of possible sensitivity to neutrino oscillation phenomena.

A new approach is therefore required to further scientific knowledge in this area. A new generation experiment is needed to follow up on the LSND result. This LDRD effort has extended the technology developed for the LSND detector at Los Alamos towards a new generation of neutrino production and detection

Scientific Approach and Accomplishments

Neutrino Source Studies Overview

The LSND signal for neutrino oscillations, in conjunction with other experiments, points to a particular dm**2 range: 0.1-2 eV**2. In order to explore this signal further a higher rate of oscillation events is necessary. A new neutrino source/detector is therefore desired that will yield a much higher rate of these events. In addition, it is important that one be able to measure the oscillation parameters precisely.

Specifically, a neutrino source should be designed with a large content of muon neutrinos, and a minimum of electron neutrinos. This is because one searches for the appearance of electron neutrinos from a muon neutrino beam, which can only occur if there is an oscillation process occurring. Fortunately, nature has provided us with the charged pion. This particle decays primarily into a muon and a muon neutrino. Only one in ten thousand decay into an electron and a background electron neutrino. A dangerous source of electron neutrino background is muon decay in flight. These neutrinos have a similar energy spectrum to the pion decay in flight neutrinos. It is again fortunate that the muon lifetime is long compared to the pion lifetime, for by keeping the decay volume short, most of the muons will not decay in flight and this background can be controlled.

An important consideration is maximizing the number of signal events while maintaining a low background. This is accomplished by using a high flux proton beam which has an energy low enough to prevent large production of K mesons. K mesons have a large decay branching fraction to electron neutrinos. The proton energy must but high enough to copiously produce charged pions. It is also advantageous to keep the neutrino energy spectrum low because this minimizes the neutral current production of pi0 events, which are difficult to distinguish from the electron neutrino charged current oscillation signal events.

Another consideration is the energy range of the neutrinos. The LSND has its maximum sensitivity at an L/E of roughly 1.0, thus, a new system would have to have a similar arrangement. The higher the energy of the neutrino beam, the further away the detector must be positioned. This can be advantageous because the background rate will fall as the inverse of the distance squared while the oscillation signal will, in the low dm**2 limit, remain nearly constant. The stops being the case when the oscillation saturates, and the oscillation signal will then die away as 1/L**2 as well. Thus the optimal location of the detector is near the first maximum of the oscillation, or L/E near 1 in our case.

There are several possible sites with accelerators in the right energy range. The Fermilab 8 GeV proton booster is a high repetition rate 8 GeV synchrotron which can deliver 15 μA of protons at a rate of 15 pulses per second. It is heavily used by the Fermilab collider program and also by the Main Injector fixed target program, but, nearly 70 percent of the potential pulses are not used. The proton beam energy is near to optimal because the kaon production rate is still low relative to the pion production rate. The booster is also kept operating with a high efficiency and reliability because it is one of the first steps in the Fermilab accelerator chain. These considerations make it an ideal candidate for a neutrino source.

Other sites would be possible such as the 28 GeV machine at BNL or the 3 GeV booster machine at KEK, but they are either less reliable, or not obviously better than the Fermilab booster.

Pion Production

Pion production by protons is the first link in a chain of processes that result in neutrino production. It is crucial to have an understanding of pion production in order to predict accurately the neutrino fluxes one may produce. There are numerous measurements of pion production at energies near the Fermilab booster's 8 GeV beam energy. Typically, measurements are interpolated between measurements at 6 GeV and 12 GeV.

There are several models available for pion production that can be used to interpolate between energies. The FLUKA code is one such model, others include the MARS program, and some p-A models which are used to model heavy ion collisions. Figure 1 shows a comparison in momentum and transverse momentum of the FLUKA predictions and the MARS predictions for π^+ production at 8 GeV on a thick copper target. There are significant differences the predictions. It will be shown later that these differences are not so relevant for neutrino production in the energy range of interest here. It should be noted that the predictions are in reasonable agreement in the most relevant energy pion range of 1-3 GeV.

Secondary Beam Transport

Once the pions are produced they must be transported until a reasonable fraction of the pions decay. The 24 ns lifetime of the pion times the relativistic time dilation of E_π/m_π (about 10) requires the pions to live around 240ns, or travel a distance of about 80 meters for a reasonable decay probability of the pions. In our case, we have chosen to lower our ν_e background from muon decay by shortening the decay tunnel slightly. This also reduces the cost of the decay tunnel. Thus 50m is used as the default decay tunnel length. The final oscillation measurement is relatively insensitive to the final tunnel length while the tunnel cost is directly proportional to its length.

Protons of 8 GeV which are incident on a target of aluminum produce pions at angles of up to 20 degrees or more. Figure 2 shows a scatter plot of the production angle versus the momentum of the pions that are produced on an aluminum target. It is important to devise a transport system that efficiently carries these pions down a long decay tunnel by focussing them to a parallel beam.

The magnetic horn system that was used at Brookhaven National Laboratory for the E746 neutrino experiment is a design that was optimized for 28 GeV protons serves as a useful model for an 8 GeV system. This system used aluminum shells with pulsed current flowing through them to generate toroidal magnetic fields around the target axis. Typical currents are 250 KA with a 1cm radius for the inner conductor surface on the first horn. The second horn serves to focus stray pions that are not focussed by the first horn and give them a second chance to be focussed.

There are a number of considerations which must be taken into account when scaling to the operating environment of the Fermilab booster. The repetition rate of the BNL system was around 0.5 Hz while the Fermilab system must be pulsed at 5 Hz on average. This implies a much higher power load. In addition, the pion energy spectrum is lower and it is necessary to change the horn configuration to accommodate this.

In order to model the secondary beam transport, the GEANT 3.21 transport code was chosen because it contains the relevant physical processes of concern: hadronic interactions, multiple coulomb scattering, electromagnetic processes, and particle decays. It is also tracks particles in non-uniform magnetic fields and thus can form a basis for a detailed simulation of the pion production, transport, and decay. This allows for an accurate prediction of neutrino fluxes from a source such as this.

Figure 3 shows a simulation of the production, transport and decay of pions and other particles from one 8 GeV proton interaction. The positively charged particle trajectories are bent towards the beam axis while the negatively charged particles are bent away from the beam axis. All relevant interactions of particles with the material of the horn system are taken into account in the simulation.

The Neutrino Flux

Neutrinos result from the decay of pions, kaons, and muons as they are transported down the decay tunnel. The pions have simple two-body decay into a muon and a muon neutrino. The kaons decay in both a two-body mode into a muon and a muon neutrino, and a three body mode into a pion, an electron, and an electron neutrino. The muon decays into an electron, an electron neutrino, and a muon neutrino. These decay chains are the major sources of neutrinos in the secondary beam. The results are shown in Figure 4 where the predicted fluxes at 500 meters from the neutrino source are 1.88 nu/pot/cm**2. Variations in the horn parameters are listed in Table 1. Figure 5 shows the flux variation as a function of the cosine of the angle from the beam axis. The change in the energy spectrum when the distance from the source is moved from 500 meters to 1000 meters is shown in Figure 6. The dependence follows a 1/r**2 behavior which demonstrates the source is acting nearly as a point source at these distances.

As a test of the package we have simulated the expected fluxes from an experiment that was performed at Brookhaven National Laboratory (Ref. 4). The agreement with the measured neutrino flux is excellent over most of the energy range as seen in Figure 7. A low energies, there are differences in the target/horn configuration which can explain the 10 percent disagreement with the predictions.

Summary

A package for calculating reliably neutrino fluxes from proton interactions on thick targets with magnetic horn focussing has been developed. This can serve as a tool for designing future higher energy neutrino experiments to explore the physics of neutrino oscillations.

Neutrino Detector Studies

The LSND System at Higher Energies

One of the most important issues addressed by this effort is whether or not it is possible to use the neutrino detection technology developed for LSND at higher energies, or whether it is necessary to abandon those in favor of a newer technology. The main issues are the scaling laws for equipment cost versus detector mass, background rejection, and how much scintillator is necessary in the mineral oil.

The LSND experiment is described in (Ref. 5). The detector consists of a cylindrical steel tank containing nearly 170 tons of mineral oil (CH_2). The mineral is doped with 0.031 g/liter of b-PBD scintillator to enhance light production 2.2 MeV neutron-capture gamma rays. This was a major component of the primary neutrino oscillation signal for the LSND experiment. In LSND, the primary neutrino source is muons decaying at rest. These neutrinos have energies up to 52.8 MeV. Furthermore, one of the main background, due to the large 7 percent duty factor, is cosmic ray produced neutrons which enter the LSND tank.

Electron-neutron separation was one of the primary goals of the LSND technology. This was accomplished primarily by measuring the time distribution of light emitted by interacting particles in the tank. When relativistic electrons lose energy in the mineral oil plus scintillator solution, almost two thirds of the light generated is prompt light (within a few nano-seconds of the primary event) from Cerenkov radiation. The remaining one third of the light is scintillation light, whose emission time has a characteristic 30 ns exponential time constant. Neutrons on the other hand generate mostly scintillation light. The time distributions of the emitted light were a reliable discriminator between electron events and neutron events.

At higher energies this capability is no longer as useful since most of the backgrounds are from sources other than neutrons, such as pi-zero decays, or muons. In general, these relativistic backgrounds have the same prompt light distribution as the signal. In addition, observing 2.2 MeV neutron capture gamma rays is no longer relevant. Thus, a detector with much less scintillation light could be considered.

One of the main issues is how much scintillation light is produced in pure mineral oil. Then, whether or not the signal can be extracted from the background neutrino processes in the presence of this scintillation light, and to find the optimum level of scintillation light for a detection system.

Pure Mineral Oil Tests

Data were taken in August of 1993 with the LSND tank filled with pure mineral oil before the b-PBD scintillator was added. The trigger for this first data run of LSND

consisted of a stopping cosmic-ray muon trigger that required a cosmic-ray muon that fired the veto shield followed by a decay electron. Figures 8 and 9 are event displays for a typical stopping cosmic-ray muon and correlated decay electron. The tank has been unfolded onto two dimensions, and each circle corresponds to a hit PMT with area proportional to the PMT charge. Note that the 40 MeV electron in Figure 9 is, roughly speaking, similar to what a 100 MeV electron will look like in a high energy detector because the LSND and a high energy detector PMT area coverages are 25\% and 10\%, respectively. Figure 10 shows the muon decay time and the phototube charge and multiplicity distributions for the triggered decay electrons, while Figure 11 shows the x,y,z spatial distributions of these decay electrons, where y is vertical and z is approximately along the neutrino direction. The measured charge per electron energy was about 10 photoelectrons/MeV, which is about 1/3 the light output of the final LSND mixture of mineral oil plus 0.031 g/l of b-PBD. Figure 12 shows the time distribution of the measured light relative to the fitted event time. About 3/4 of the light is in the main Cerenkov peak, while 1/4 of the light is scintillation light with a time constant of about 35 ns. This information is included in the detector simulation that is discussed in the following chapter. Note that mineral oil scintillates due to impurities that necessarily occur in the oil. The 3 to 1 ratio of Cerenkov to scintillation light is close to optimal for event reconstruction and particle identification. There is sufficient late light to measure the scintillation light fraction but sufficiently little isotropic light so as not to obscure the Cerenkov cone. We have the capability of adding b-PBD scintillator to the oil to increase the scintillation fraction, and the precise amount of scintillation light over time can be determined from the fraction of late PMT hits.

The issue of whether or not pure mineral oil (MO) produces scintillation light appears to have no simple answer as MO is not a well characterized substance. The linear chains that constitute the bulk of a MO sample do not facilitate the development and propagation of visible light arising from the stopping of charged particles via collisions with electrons in the oil. However, if traces of benzene-like rings are present in the MO sample, it is possible that scintillation light will be produced and the material will be transparent to light at this wavelength. Such scintillation light would be particular to the sample being tested and can not be taken as quantitatively characteristic of MO. The material's history and trace contaminates will dominate the scintillation light characteristics. To investigate its suitability for a high energy detector, measurements of the scintillation light produced by the MO used as the base in LSND were carried out. This sample of MO contained no known additives and had been in storage under dry nitrogen at Los Alamos for about 5 years. The samples were exposed to 120 MeV deuterons from the Texas A&M

Cyclotron and the light detected in a 5cm diameter Phillips XP2232B PMT. Figure 13 illustrates the set up. The deuteron beam (~1500 d/sec) emerged from the beam pipe, passed through a thin (1mm) trigger scintillator and then traversed the 5 cm inner diameter of the cylinder containing the MO. The 120 MeV deuterons lost an average of 57 MeV in the MO. A trigger pulse associated with each beam particle gated the A DC recording the integrated charge from the PMT. Figure 14 shows the recorded charge with the beam directed along a diameter 1 cm in front of the face of the PMT, with the cylinder filled with air, water, and MO respectively. There is a clear signal of scintillation light from MO and none from the air or water. Figure 15 shows the measured charge as a function of distance between the beam trajectory and the face of the PMT expressed as the average number of detected photoelectrons (PE). The number of detected PEs is observed to be directly proportional to the solid angle of the beam path subtended by the PMT. A fit to the data reveals 0.83±0.07 PEs/MeV of beam energy loss. The average number of PEs created by these traversing deuterons is approximately 14\% of the number created by Cerenkov radiation from a fully relativistic particle traveling the same path. Figure 16 is the PMT output for a single passage of a beam particle as recorded by a Tektronix TDS 620. The upper trace is the signal from the trigger while the lower trace shows the PEs from the MO sample. The horizontal scale is 20ns/div. The PE time distribution is consistent with a scintillation decay time of about 30 ns .

Another sample of MO from an entirely different source was tested and it produced similar results except that the light output was 3 times lower. However, the decay time of the scintillation light was approximately 30 ns, consistent with the above sample. Thus, it appears that commercial samples of MO do scintillate and the scintillation light will be appreciably delayed relative to prompt Cerenkov light, although the amount of light varies depending on the sample and will have to be measured before use in an experiment such as a high energy detector.

Simulation of a High Energy Detector

A high energy detector was simulated using the GEANT Monte Carlo package. A spherical tank filled with mineral oil was coded into the program with dimensions of 10 meters in diameter. An approximation of a PMT was modeled and multiple copies were positioned as shown in Figure 17.

The GEANT implementation (V3.21) simulates the production of Cerenkov light for particles with velocities above threshold and tracks this light through the media using the (wavelength-dependent) optical properties of the mineral oil. This optical photon tracking was also used to track scintillation photons that were generated isotropically and in

proportion to the amount of energy lost by charged particles in the mineral oil. These optical photons were tagged as Cerenkov or scintillation photons so that the amount of scintillation light could be adjusted in the reconstruction phase. If an optical photon intersected the photocathode surface of the PMT volume, it was detected with an efficiency equal to the wavelength-dependent quantum efficiency of the PMT. These PMT hits were written to an ntuple along with the veto and input particle information.

In order to study the response of the proposed detector, first, single particle muon, electron, and pi^0 events were generated isotropically over a range of energies (50-2000 MeV) within the mineral oil volume of the inner tank. Then, to better understand the relative rates for the signal and background reactions, multi-particle events of interest to the a high energy detector experiment were simulated. The most important reactions studied were: $\nu_e C \rightarrow e^- X$, $\nu_\mu C \rightarrow \mu^- X$, and $\nu_\mu C \rightarrow \nu_\mu \pi^0 X$. The final states of these reactions often include an energetic proton which was included in the simulation. These events were generated within the fiducial volume of the inner tank and were weighted by the estimated cross sections and neutrino fluxes.

Event Analysis

The purpose of this section is to provide an intuitive understanding of events in the detector. The technical description of how this information is used is found in the following sections of this chapter. The general ideas behind event reconstruction in Cerenkov counters have been developed in a wide range of experiments, including LSND, IMB, Kamioka and Super Kamiokande.

This detector records information on:

- The phototube which was hit
- The timing of the initial hit for each tube
- The number of photoelectrons
- The veto hits in an event.

Based on this information, events can be reconstructed, (*i.e.* mean track position and direction determined) and particles identified, as summarized in Table 1. The mean position of the track is required to be within the fiducial volume of the detector.

Table 1

Some principles of particle ID in a high energy detector

	Cerenkov Ring	Track Extent	Timing of hits
electrons	$\beta \sim 1 \rightarrow \alpha = 45°$, fuzzy ring	short track	More prompt than late light
muons	sharp outer edge of Cerenkov ring	long track	high fraction of late light
π^0's	two rings	extended source region	energetic recoil proton produces scintillation light

The main goal of the event reconstruction and particle identification is to separate quasi-elastic ν_e scatters producing an electron from the background of muons and single π^0s. As illustrated in Figure 18, electrons, muons, and neutral pions have quite different topologies in the tank. In general, most muons are identified by the veto. Most muons which stop in the detector will decay, however 8\% will be captured. Decay muons are identified by two tracks (as shown in Figure 18). Stopped muons which capture must be identified by their signature of photons in the tank, as discussed below. Those muons which are not cut represent a background to the analysis. In general, neutral pions are identified as having two electromagnetic tracks, one from each photon. Highly asymmetric decays represent a background to the analysis. Cerenkov and scintillation light are produced by charged particles above threshold in the detector. For the case of electrons, the detector sees around 75% Cerenkov light and 25% scintillation light. The Cerenkov light will form a ring while the scintillation light is isotropic. Because the scintillation light results from atomic transitions, these photons have a high probability of arriving at the phototubes later than the Cerenkov light in an event, which is, therefore, described as "prompt". Thus both the ring and the timing distinguish the scintillation light from the Cerenkov photons.

The direction and angle of the track can be reconstructed based on minimizing the difference between timing and position of phototube hits with respect to a hypothesis track. Consider a track which is traveling faster than the speed of light in the oil. For the case of tubes downstream of the track, photons from the downstream end of the track will

arrive before those from the upstream end. Also, the Cerenkov ring will have a smaller radius for photons from the downstream end compared to the upstream end. When discussing "late" or "early" hits, this is with respect to the timing of the midpoint of the reconstructed track. Thus for an extended track, photons from the downstream end are most likely to arrive early. Typically, a charged particle will produce thousands of photons.

Intuitive information can be gained from considering event displays. An event display has not been written for a high energy detector, however the LSND event display is instructive for electrons (Figure 9) and muons (Figure 8). These data were taken with pure mineral oil in the LSND detector, as discussed in section 5.5, above. Hits are color coded to represent timing information.

Electrons have relatively short tracks and are at $\beta \sim 1$. So naively one would expect these particles to produce well defined Cerenkov rings with opening angle $\alpha = 47°$ in mineral oil. However, multiple scattering and bremsstrahlung typically smear the ring associated with an electron. The electron remains above Cerenkov threshold throughout most of its path in the detector, thus the photons are predominately prompt.

The track length is useful for identifying muons. Many muons will exit the detector firing the veto tubes. The timing and position information for the hits associated with a muon will combine to indicate an extended source or, in other words, a long track. Muons which traverse the detector produce hits in nearly all of the phototubes. Lower energy muons may decay within the detector. In this case, the track reconstruction will indicate the presence of the initial track followed by the secondary track from the electron.

When running with a neutrino beam, μ^- are produced by the quasi-elastic scattering process and 8% of these muons are captured in the oil. These muons can be distinguished from electrons through the distinctive Cerenkov and scintillation signatures. Initially, most muons will be of sufficiently high energy that $\beta \sim 1$, producing a Cerenkov ring consistent with $\alpha = 47°$. Because muons suffer less multiple scattering than electrons, the outside edge of this Cerenkov ring remains sharp. However, as the muon slows in the oil, the Cerenkov angle becomes smaller, thus the inner region of the ring fills in with photons. The muons will drop below threshold earlier than the electrons, resulting in a larger fraction of late to prompt light in a muon event. The hits can be compared in Figures 8 and 9 for data from LSND.

Recoil protons from the quasi-elastic interactions are below Cerenkov threshold. Thus they produce only scintillation light. Showers from photons and electrons are indistinguishable in the detector. However, there are several handles for separating π^0 events with two photons from the electron events which form the signal. In most cases, the opening angle is sufficiently large to produce two distinctive Cerenkov rings in the detector. The photons may convert at some distance from the interaction vertex. As a result, the source of the photons is reconstructed to be from an extended vertex region. Also, single pion production events typically have more energetic recoil protons than quasi-elastic scatters, resulting in more scintillation light in the event. These signatures allow identification of most of the single π^0 events, as discussed below, leaving those cases with a highly asymmetric decay and a low energy recoil proton.

Event Reconstruction

Events are reconstructed using a fitting algorithm developed for LSND. As in LSND, the chi square of the position and angle fits (χ_r and χ_a) are minimized to determine the event position and direction. In addition, these minimized chi squares, together with the fraction of PMTs with late hits (χ_t) or early hits (χ_{t0}), provide excellent particle identification and low $\mu^{\pm}$-$e^{\pm}$ and π^0- $e^{\pm}$ misidentification.

To determine the event position and time (corresponding to the midpoint of the track), the position chi square, χ_r, is minimized. χ_r is defined as:

$$\chi_r = \quad q_i (t_i - t_0 - r_i / v)^2 \; / Q$$

where q_i is the charge of hit phototube *i*, t_i is the time of hit phototube i, t_0 is the fitted event time, r_i is the distance between the fitted position and phototube i, v is the velocity of light in oil (20.4 cm/ns), Q is the total number of photoelectrons in the event, and the sum is over all hit phototubes. Similarly, the event direction (for particles above Cerenkov threshold) is determined by minimizing the angle chi square, χ_a. χ_a is defined as:

where α_i is the angle between the fitted direction and the line segment extending from the

$$\chi_a = \quad (\alpha_i - 47°)^2 \; / Q$$

fitted position to hit phototube i, 47° is the Cerenkov angle for $\beta \approx 1$ particles in mineral oil, and the sum is over all hit phototubes. Note that for both χ_r and χ_a, any PMTs that are

dead or arcing are ignored. With the track direction determined, the initial event vertex is found by using the measured track energy (which is proportional to the total number of photoelectrons in the event) to extrapolate back to the vertex.

Electron Resolutions

The event reconstruction algorithm has been tested by our detector simulation discussed above. A large sample of $\nu_e C \rightarrow e^- N$ electron events were generated uniformly in the tank in the energy range from 50 to 2000 MeV. Figure 19 shows the resulting position, angular, and energy resolutions. As can be seen in the figure, the position resolution is about 34 cm, the angular resolution is about 6° and the energy resolution is about 10\%. Note that for electron events there are about 3.8 photoelectrons per MeV.

Particle Identification

A typical event in a high energy detector will cause hundreds of PMTs to be hit, where for each PMT hit there will be recorded the time of the first photoelectron and the total charge deposited. Excellent electron identification and muon and neutral pion rejection can then be obtained by using the fraction of late PMT hits (which measures the fraction of scintillation light), the fraction of early PMT hits, and the quality of the vertex and Cerenkov cone fits. Muons can be identified and rejected usually from the decay electron. However, (8±0.1)% of the μ^- will be captured before decaying. These captured muons are rejected for several reasons. First, quasi-elastic muon events have relatively more scintillation light than quasi-elastic electron events because of the muon mass (muons have a Cerenkov threshold of 38 MeV) and the recoil protons, which are more energetic on average than for quasi-elastic electron events. Also, muons travel farther than electrons, and this results in relatively more early and late PMT hits and a worse vertex position fit. Furthermore, muons have less multiple scattering and radiation than electrons, which causes the outside of the Cerenkov ring to be sharper for muons than for electrons. The inside of the Cerenkov ring will be somewhat filled in as the muons approach the Cerenkov threshold.

Neutral pions can also be rejected easily. First, neutral current π^0 events have relatively more scintillation light than quasi-elastic electron events because of the recoil protons, which are much more energetic on average than for quasi-elastic electron events. Also, π^0s are more spread out than electrons due to the radiation of the decay γs, and this results in relatively more early and late PMT hits and a worse vertex position fit.

Furthermore, π^0s have two Cerenkov rings and relatively less charge in either of the rings than electron Cerenkov rings.

Therefore, electron events can be distinguished from muon events and neutral pion events by fitting the Cerenkov ring and event vertex and by measuring the fraction of PMTs with a late hit. Figure 20 shows χ_t, the fraction of PMTs hit after 10 ns from the reconstructed time of the event, χ_{t0}, the fraction of PMTs hit before the reconstructed time of the event, $\chi_r \times \chi_a$, and r_q, the ratio of charge deposited in PMTs with $0.5<\cos\theta<0.7$ to $0.8<\cos\theta<1.0$ (θ is the angle between the PMT direction and the fitted event direction), for electron events (solid curve), muon events (dashed curve), and neutral pion events (dotted curve). Events have been rejected with more than 60 MeV of energy in the veto shield, reconstructed time more than 5 ns from the beam time, or a second Cerenkov ring within 23° of the first ring. The relative numbers of events are normalized to what will be observed in the detector, and a clear separation is observed between electron events, μ^- events and π^0 events. The number of events remaining after successive selections is shown in Table 2. With these selections, the efficiency for electron events as a function of visible charge is shown in Figure 21, while Figure 22 shows the π^0 efficiency and π^0/e^- efficiency ratio as a function of visible charge. The π^0 events are reduced by a factor of about 200, while maintaining a 50% efficiency for electron events Note that no μ^- events have passed the selection so far. The veto region is not crucial for the PID; however, it serves as a redundant tag for tracks leaving or entering the detector.

Table 2

The number of events remaining after successive selections. The Veto, Time, Ring selection rejects events with more than 60 MeV of energy in the veto shield, reconstructed time more than 5 ns from the beam time, and a second Cerenkov ring within 23° of the first ring. Q is the total charge in the event, while χ_t, χ_{t0}, χ_r, χ_a, and r_q are described in the text.

Selection	e^- events	μ^- events	π^0 events
Total	4000	4000	4000
Veto, Time, Ring	2811	157	233
$\chi_t \times \chi_{t0} < 0.024$	2238	5	140
$\chi_r \times \chi_a / r_q < Q/1000.+1$	1952	0	19

Systematic Uncertainty on the μ^- and π^0 Misidentification Background

As discussed in the previous section, the μ^- event and π^0 event misidentification as e^- event probabilities are approximately 0.0005 and 0.005, respectively. These misidentifications occur when the μ^- is captured in the oil before decaying (the probability of capture is (8±0.1)%, while the decay electron inefficiency is less than 10^{-2}) or when the π^0 decay is highly asymmetric. Therefore, we can measure the misidentification background by applying the PID selection on μ^- that decay, ignoring the decay electron, and by measuring the π^0 symmetric decays. Figure 23 shows the cosine of the angle between the two fitted Cerenkov rings for π^0 decays (dashed curve) and electrons (solid curve). Although electrons should have only a single Cerenkov ring, multiple scattering and radiation by the electron will lead to a second ring. However, as shown in Figure 23, the cosine of the angle distributions between the two rings have much different shapes, so that the π^0 background can be well measured. We, therefore, will be able to measure the μ^- event and π^0 event misidentification backgrounds with a systematic error of 5\%.

Conclusion

This R&D effort has demonstrated that the technology that was developed for the LSND neutrino oscillation experiment can be extended to the next generation neutrino experiment at Fermilab. This will allow Los Alamos to continue to play a leading role in this exciting field of science. We have determined that a high intensity, multi-GeV proton beam can provide sufficient neutrino flux for a precision measurement of the oscillation parameters observed by LSND. This can be accomplished by a magnetically focussed secondary beam of pions that are allowed to decay in a 50 meter decay tunnel.

Neutrino detection and measurement can be accomplished by an extension of the LSND detector system where the scintillator is left out of the mineral oil, enhancing the ratio of Cerenkov light to scintillation light produced by relativistic charged particles in the liquid. The resulting system will be able to achieve the required rejection of neutrino induced backgrounds from muon neutrino charged current and neutral current interactions. This will allow a sensitive determination of the LSND oscillation signal.

References

1. C. Athanassopoulos *et al*, LSND Collaboration, Phys. Rev. **C54**, 2685 (1996)
2. R. Maschuw, *et al*, KARMEN Collaboration, Prog. Part. Nucl. Phys. **40**,
3. C. Athanassopoulos *et al*, LSND Collaboration, Phys. Rev. **C81**, 1774 (1998)
4. L. A. Ahrens *et al*, Phys. Rev. **D34**, 75 (1986)
5. C. Athanassopoulos *et al*, LSND Collaboration, NIM **A388**, 149 (1997)

Publications

1. E. Church *et al*, LAUR-98-352
2. E. Church *et al*, LAUR-99-1892
3. C. Athanassopoulos *et al*, LSND Collaboration, Phys. Rev. **C81**, 1774 (1998)

Figure Captions

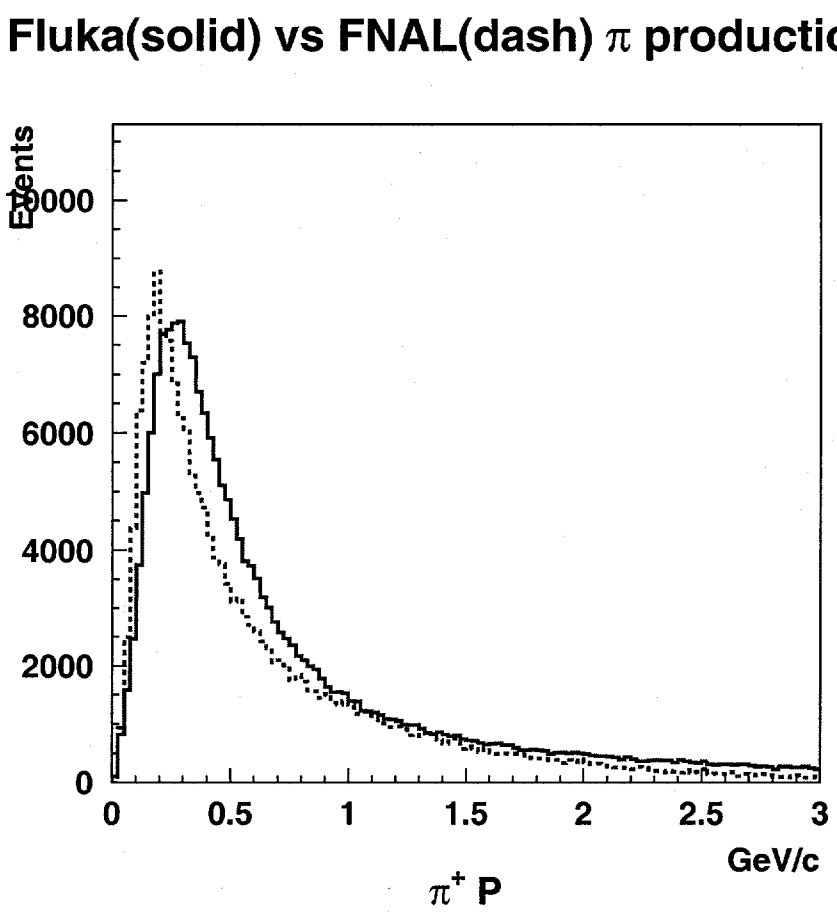

Figure 1. A comparison of the FLUKA and MARS predictions for pion production on a copper target. The total momentum is shown for 8 GeV protons on target.

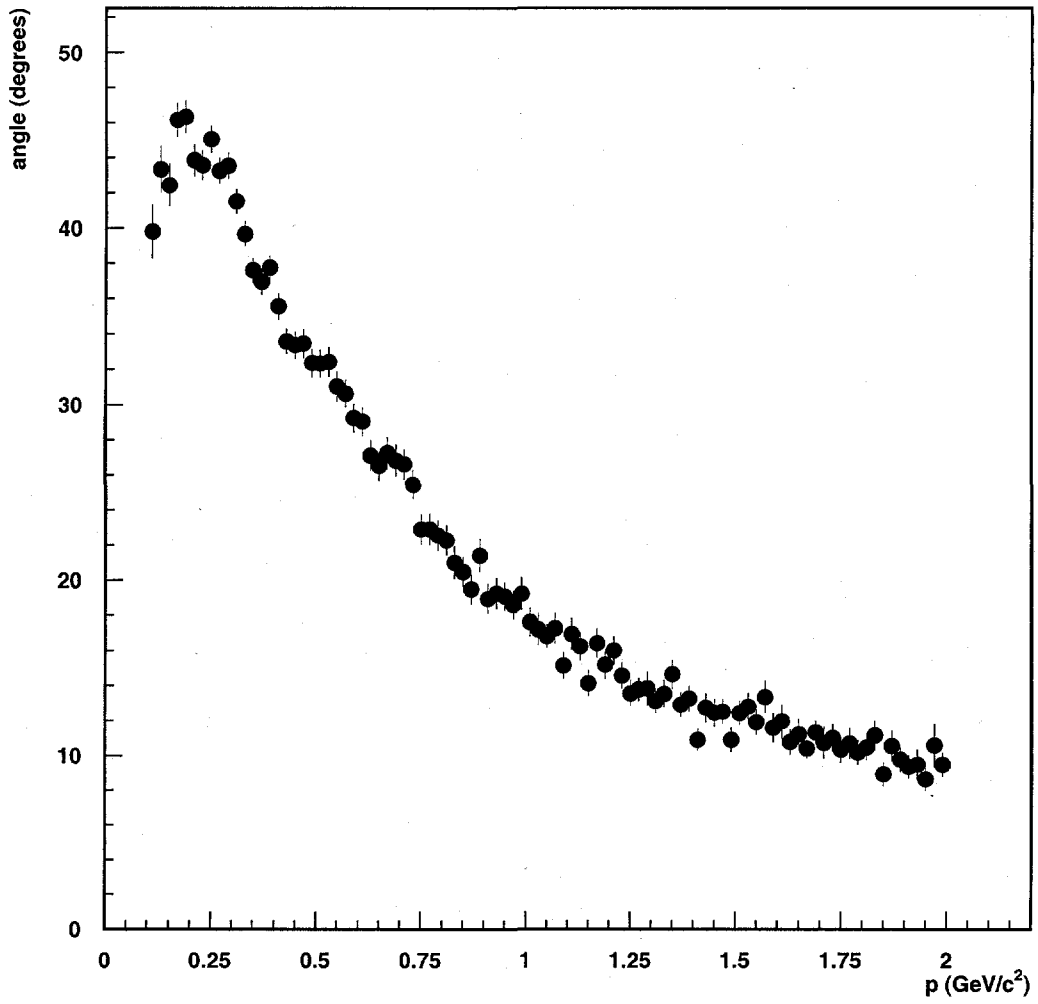

Figure 2. Pion production angles versus momentum of the pion.

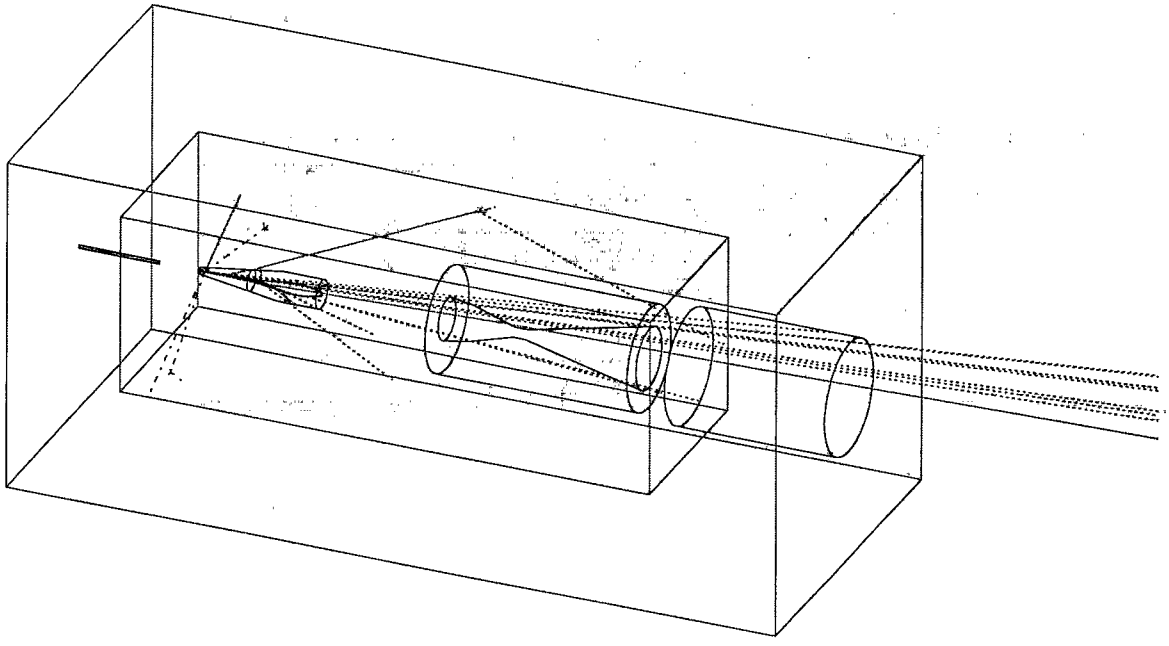

Figure 3. An 8 GeV proton interaction in the magnetic horn simulation.

Figure 4. Flux of muon neutrinos (solid histogram) and electron neutrinos (dashed histogram) from a 50m decay length beam line at 500 m and 1000 m from the target.

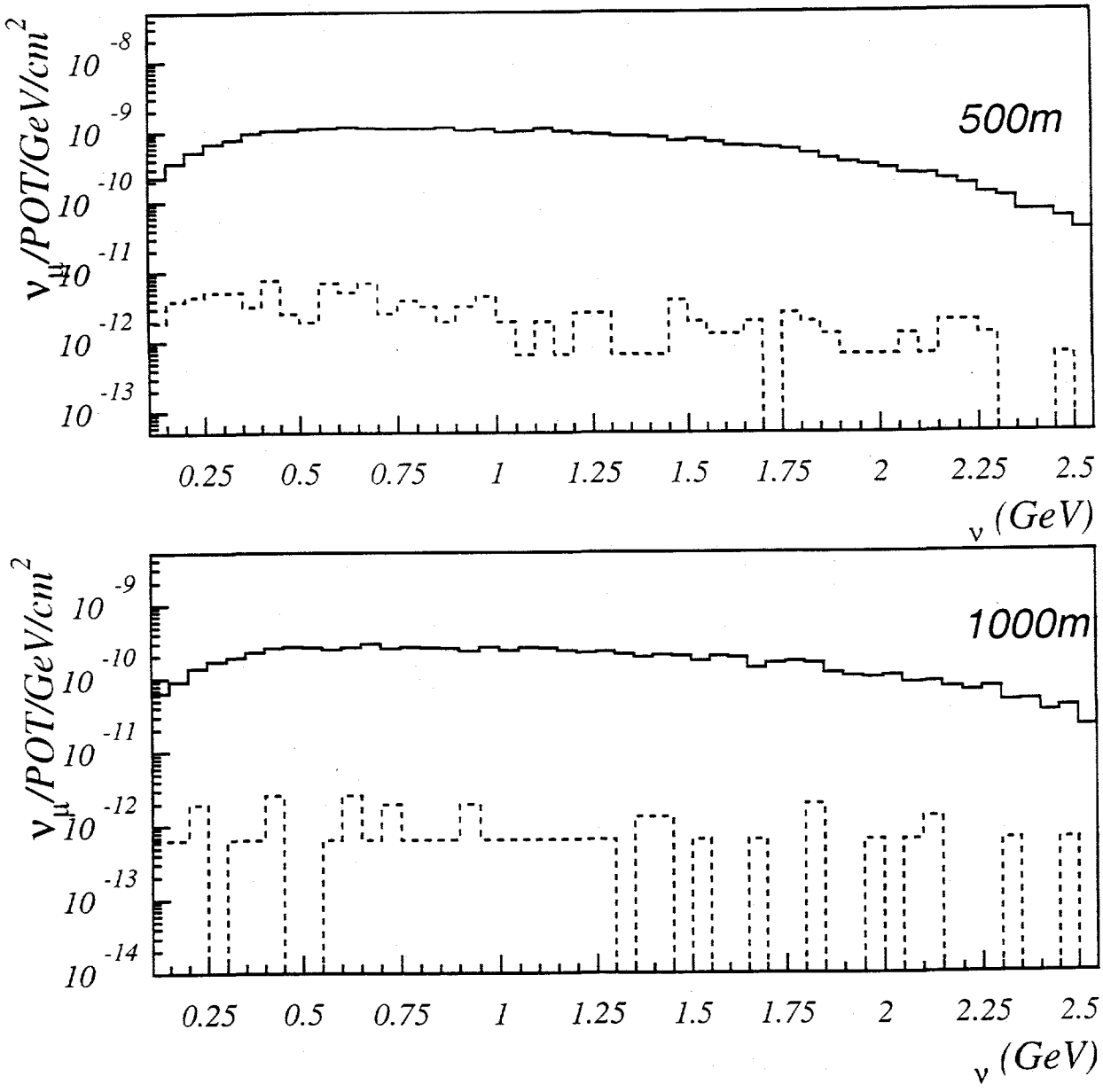

Figure 5. The neutrino flux as a function of neutrino energy (GeV) and cosθ , where θ is the angle of the neutrino relative to the incident proton direction.

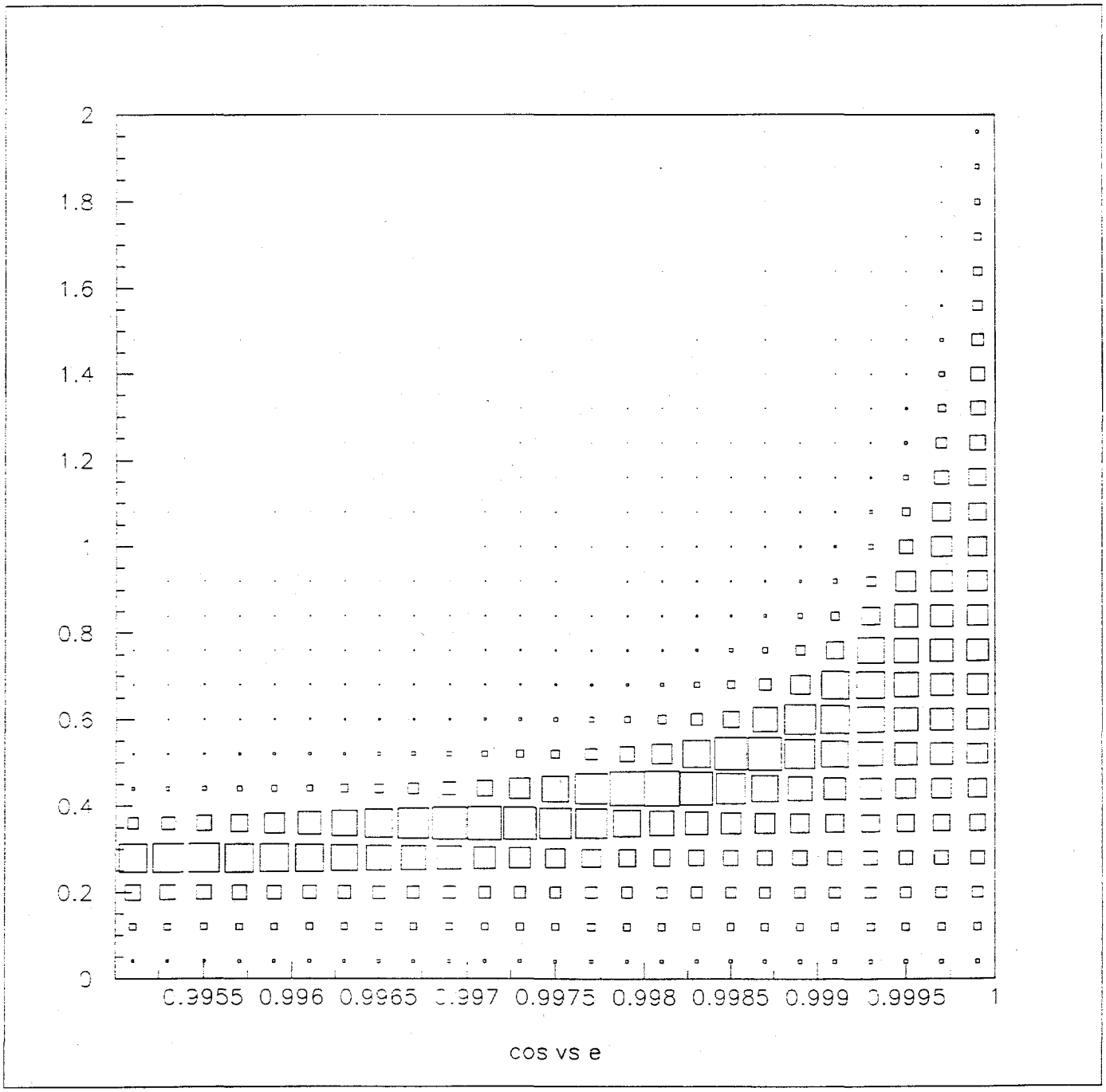

Figure 6. The ratio of the neutrino flux passing through a high energy detector at 1000 m compared to 500 m as a function of neutrino energy in GeV. The ratio is normalized such that it equals one for a pure 1/r**2 dependence. The upper figure shows the full energy range, while the lower figure enlarges the region of interest.

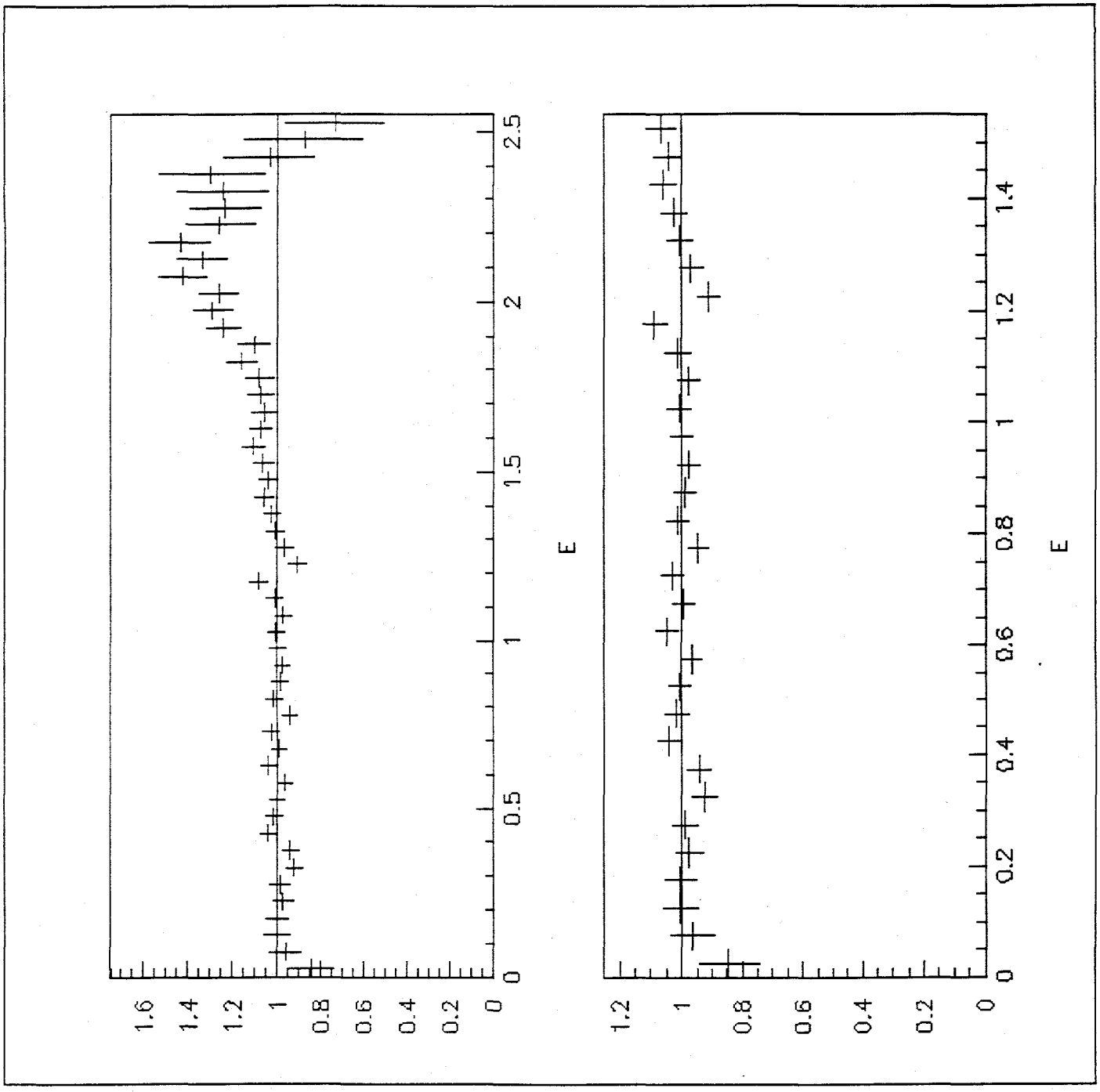

Figure 7. The BNL measured flux for 28 GeV protons on target compared to the flux from the GEANT simulation of that neutrino source.

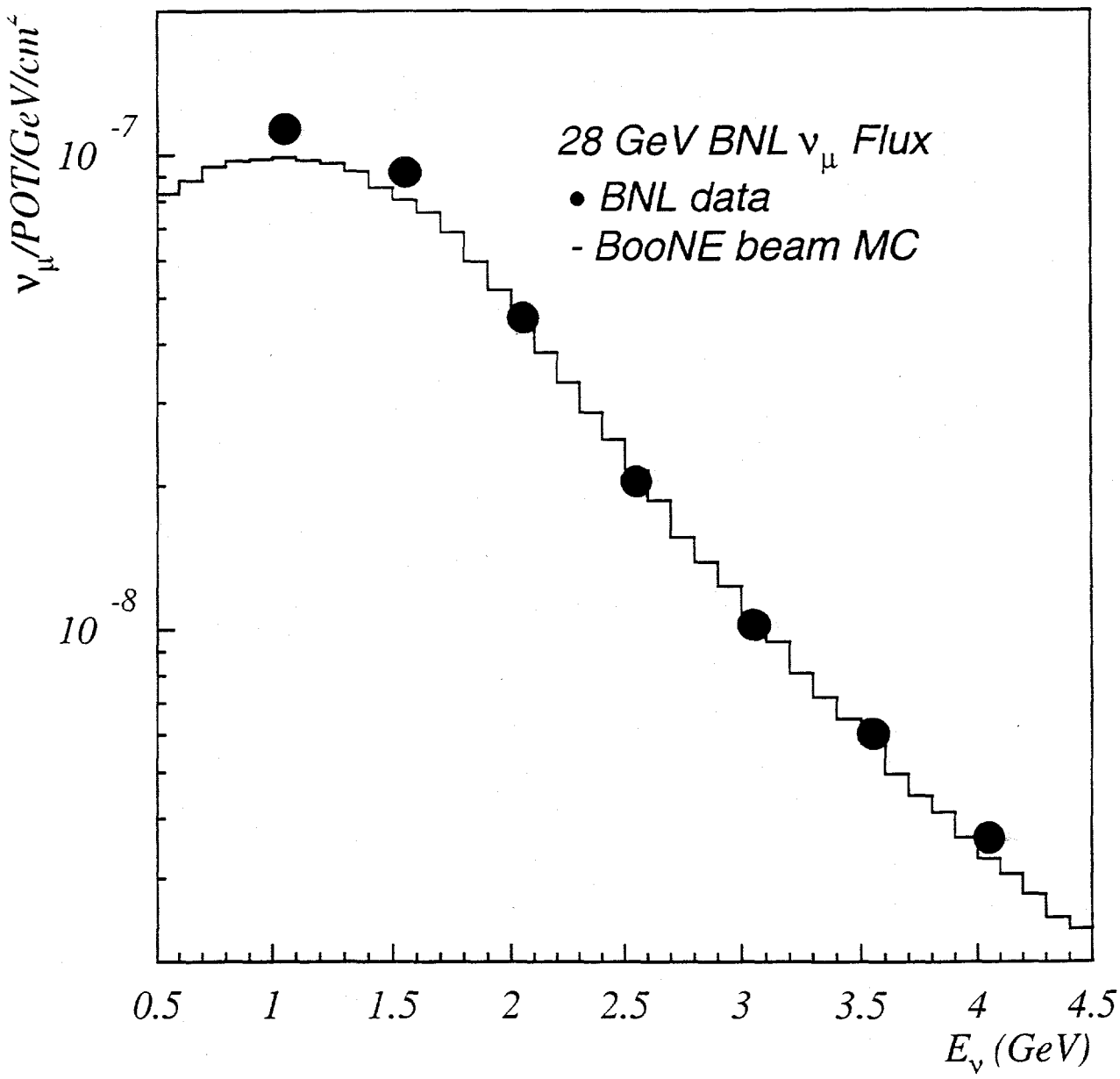

Figure 8. The event display for a typical stopping cosmic-ray muon. The tank has been unfolded onto two dimensions, and each circle corresponds to a hit PMT with area proportional to the PMT charge.

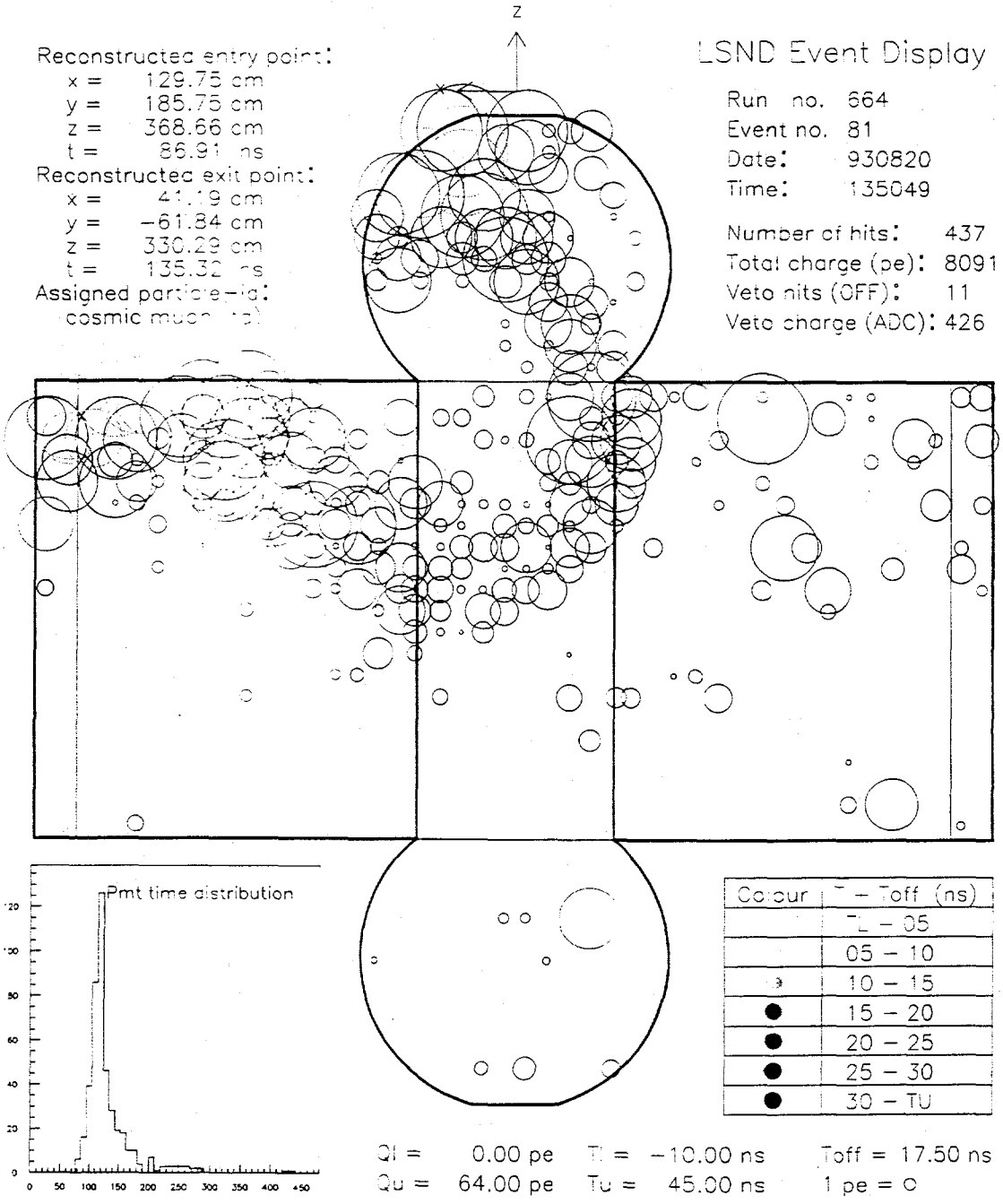

Figure 9. (electron13.eps) The event display for a typical decay electron. The tank has been unfolded onto two dimensions, and each circle corresponds to a hit PMT with area proportional to the PMT charge.

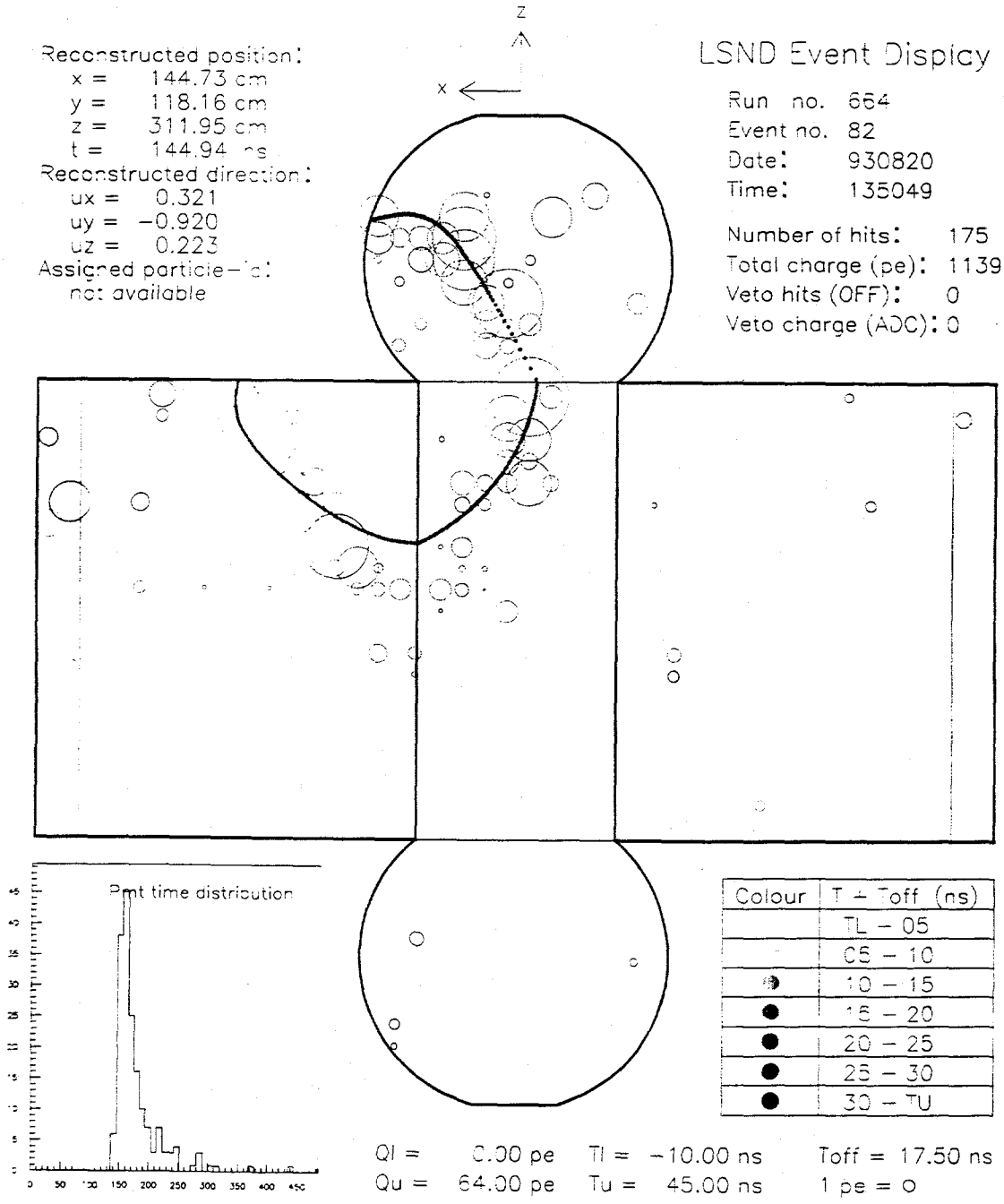

Figure 10. The muon decay time and the phototube multiplicity and charge distributions for the triggered electrons from muon decay.

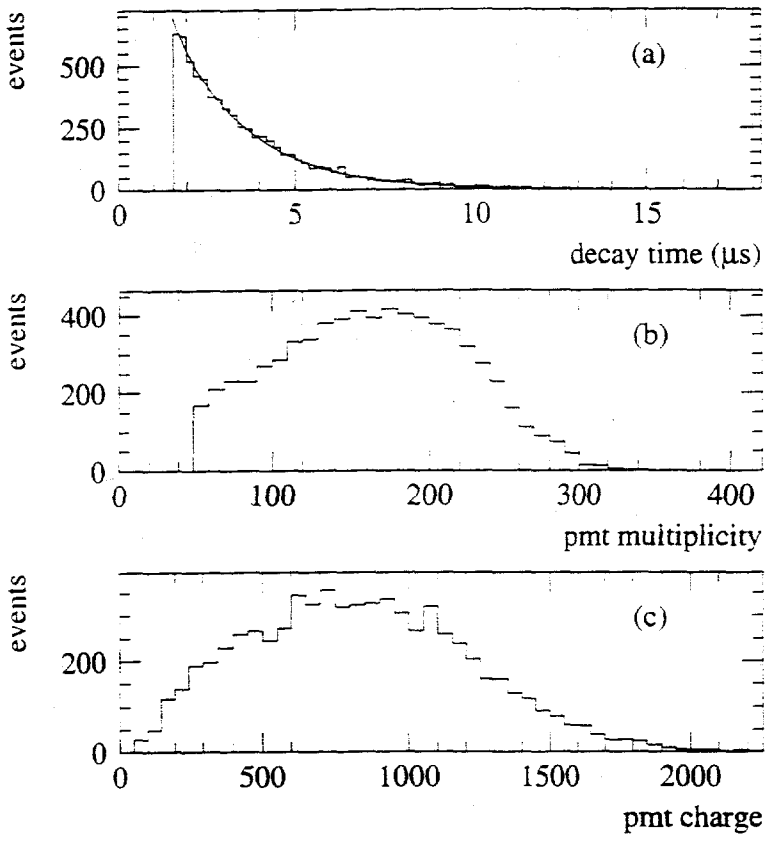

Figure 11. (xyz_664.eps) **The x,y,z spatial distributions of the electrons from muon decay, where y is vertical and z is approximately along the neutrino direction.**

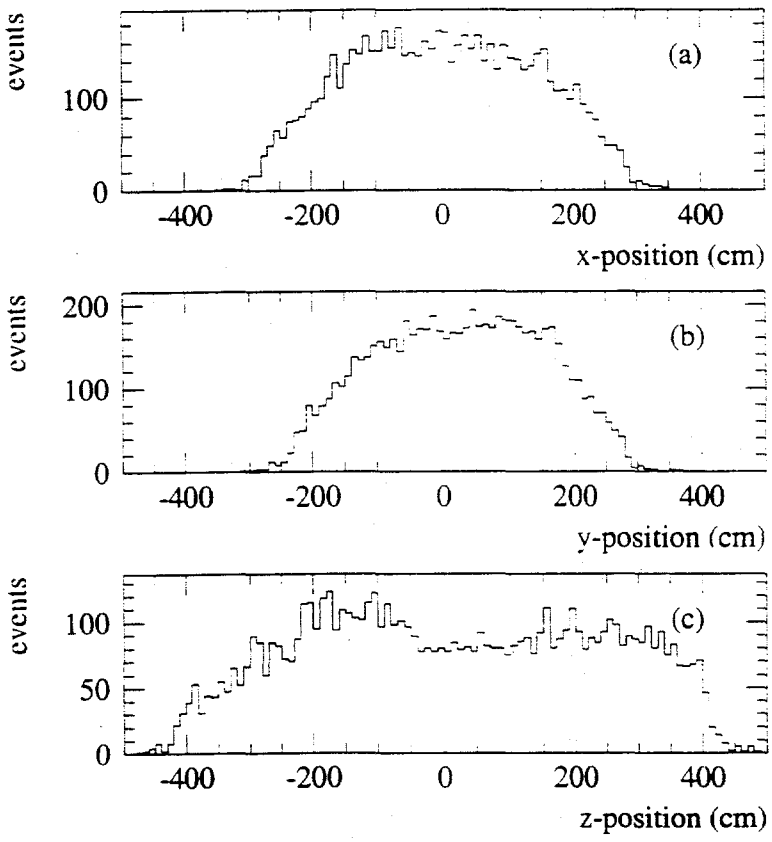

Figure 12. (time_664.eps) **The time distribution of the measured light of electrons from muon decay relative to the fitted event time.**

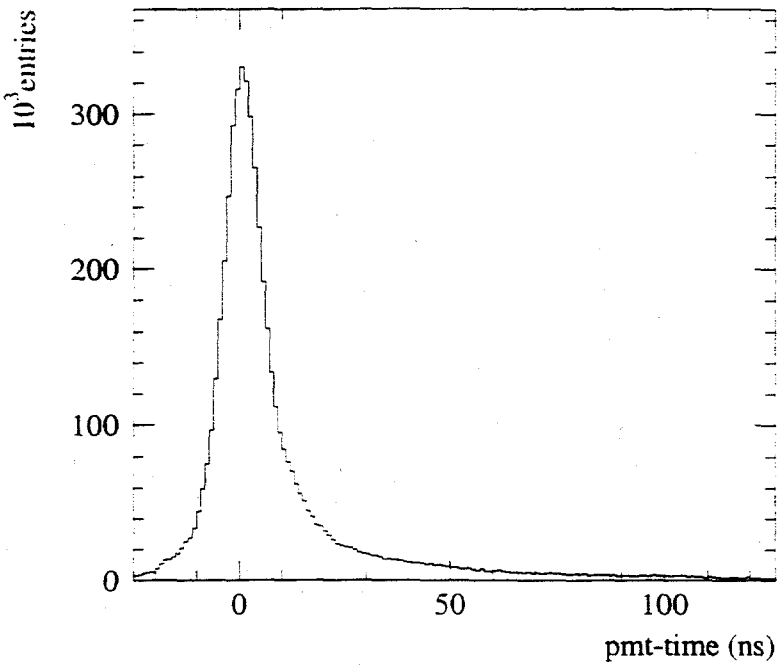

Figure 13. (mo_fig1.eps) An illustration of the setup for the tests at the Texas A\&M Cyclotron.

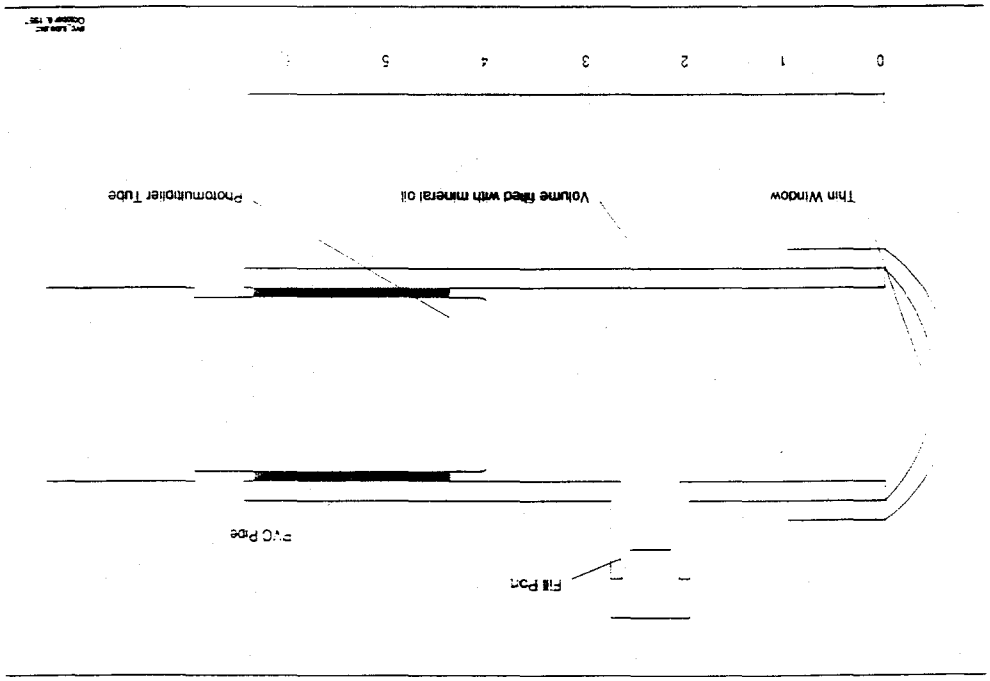

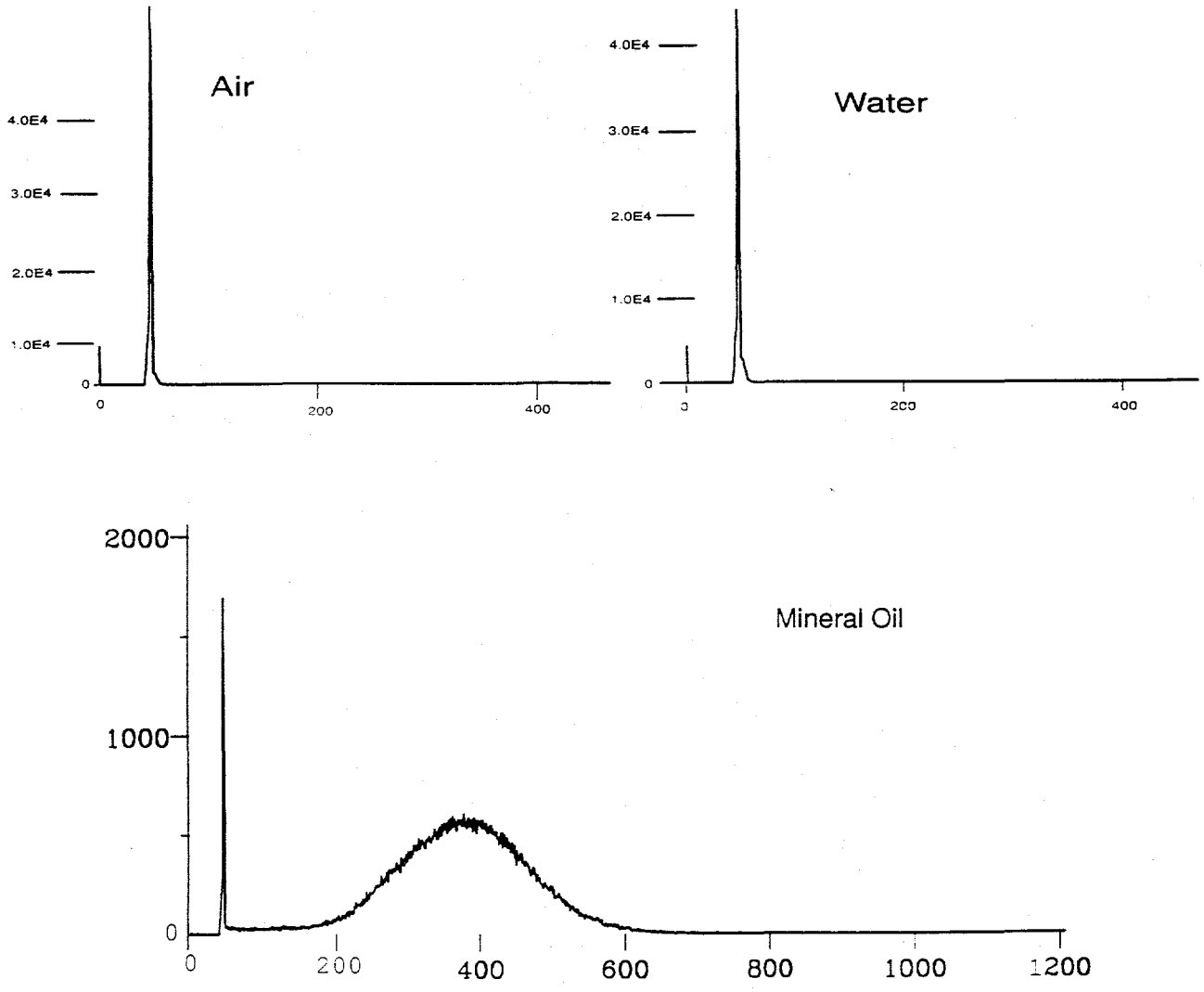

Figure 14. The recorded charge with the beam directed along a diameter 1 cm in front of the face of the PMT, with the cylinder filled with air, water, and MO respectively.

Figure 15. The measured charge as a function of distance between the beam trajectory and the face of the PMT expressed as the average number of detected photoelectrons (PE).

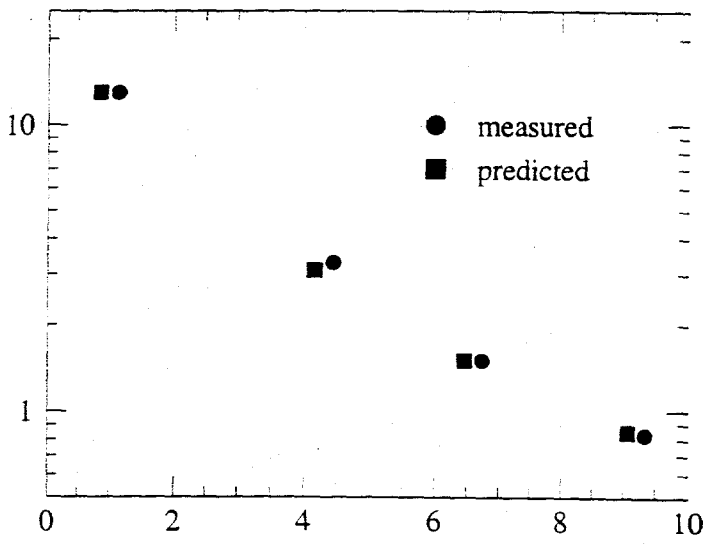

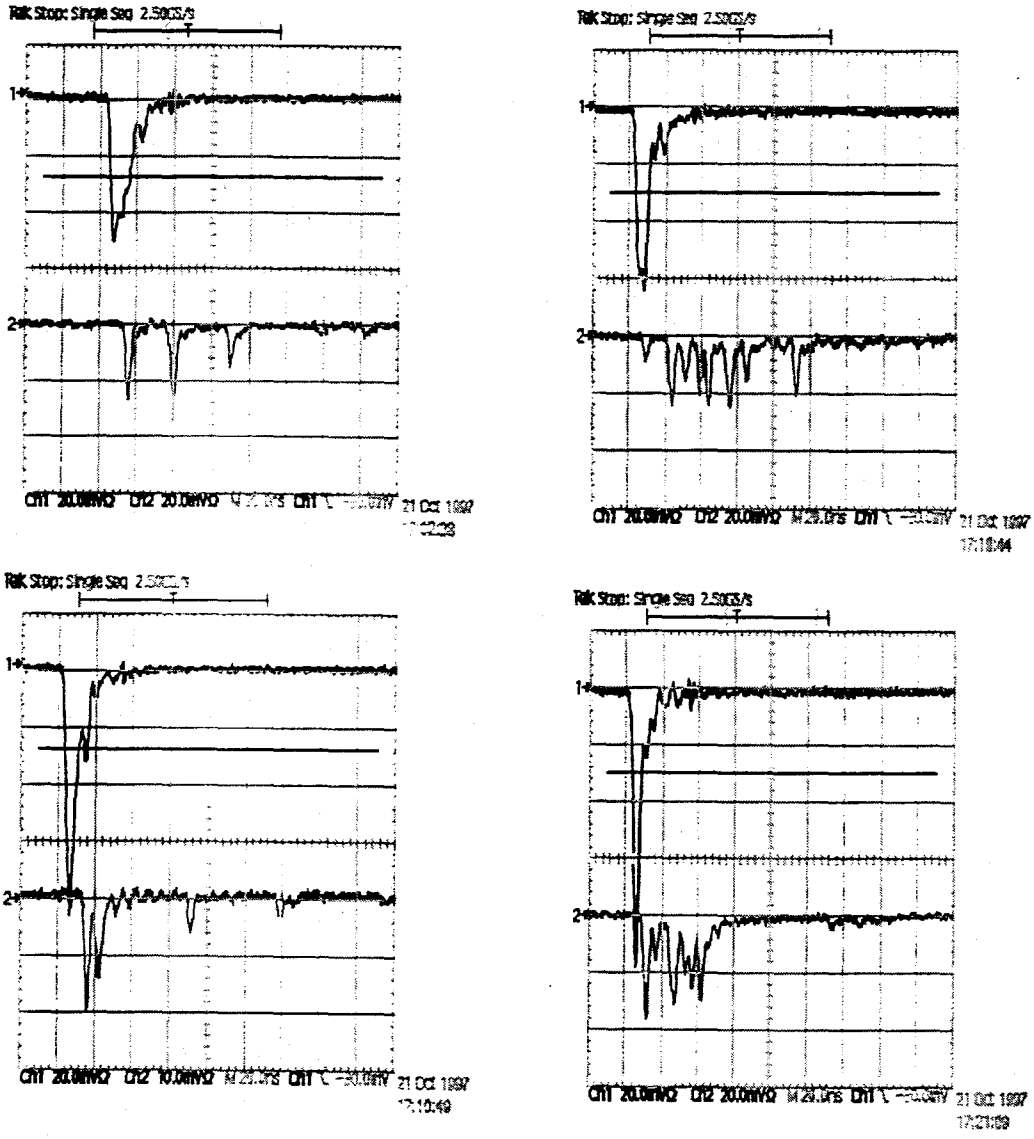

Figure 16. (mo_fig4.eps) The PMT output for a single passage of a beam particle as recorded by a Tektronix TDS 620. The upper trace is the signal from the trigger while the lower trace shows the PEs from the MO sample. The horizontal scale is 20ns/div.

Figure 17. GEANT-generated schematic of a possible high energy detector.

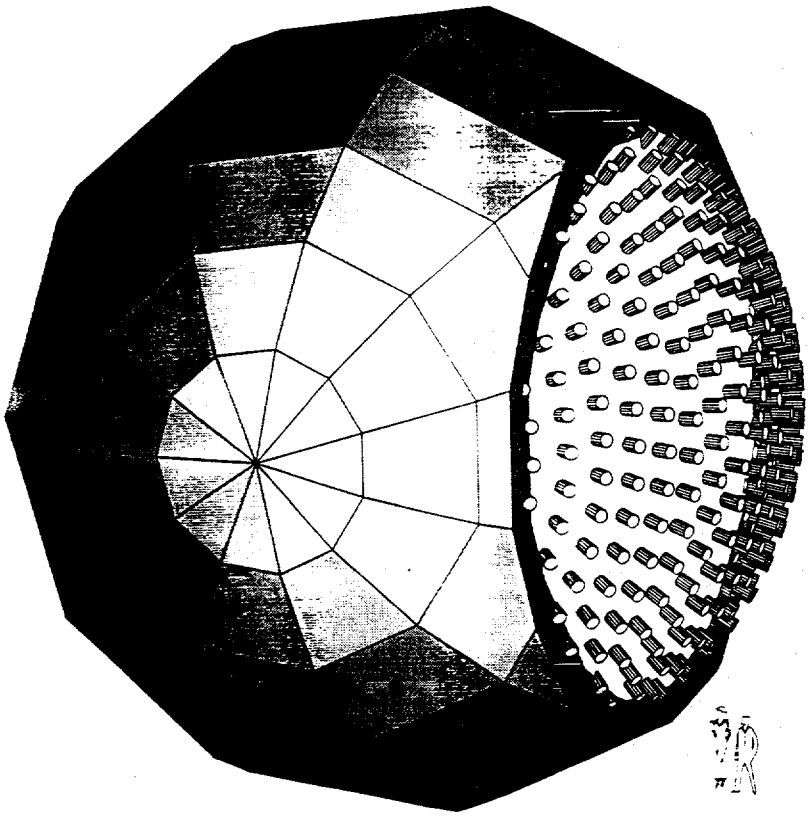

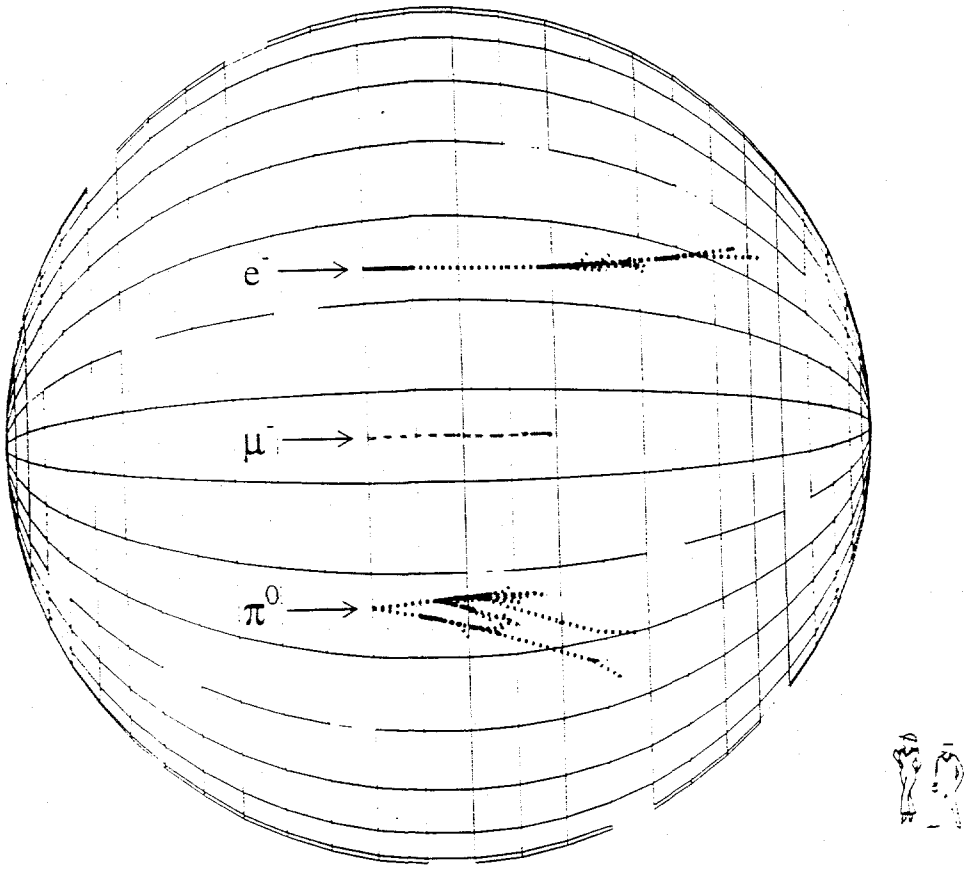

Figure 18. Example topologies of 500 MeV electrons, muons, and neutral pions in the detector tank.

Figure 19. For ν_e C interactions, the (a) position (in cm), (b) angular, and (c) energy resolutions for a large sample of electrons generated in the tank by the detector simulation.

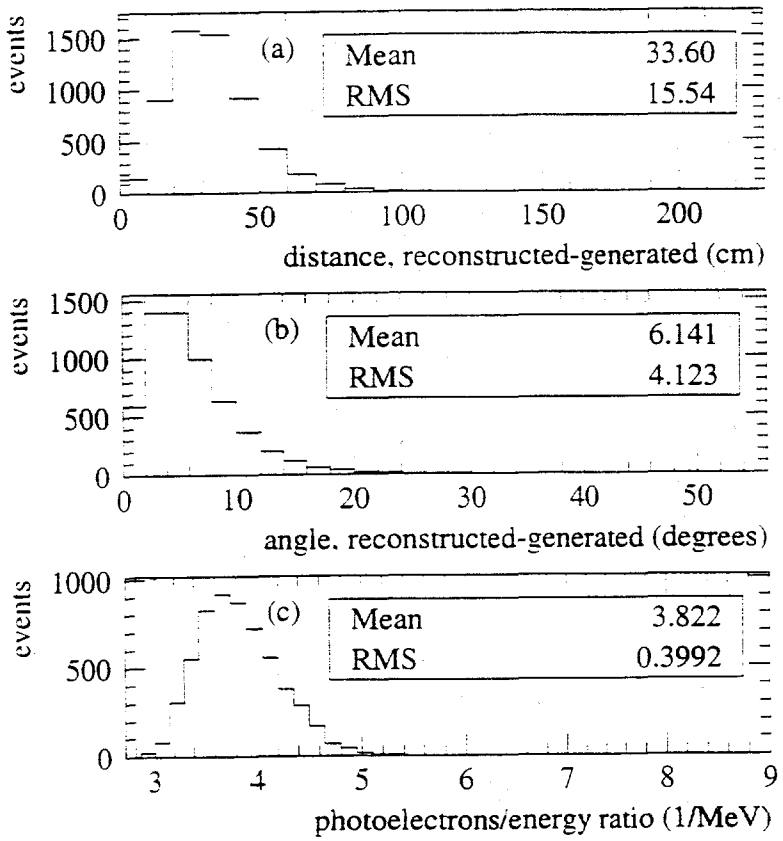

Figure 20. The (a) χ_t, (b) χ_{t0}, (c) $\chi_r \times \chi_a$, and (d) r_q distributions for electrons (solid curve), muons (dashed curve), and neutral pions (dotted curve). The relative numbers of events are normalized to what will be observed in the detector.

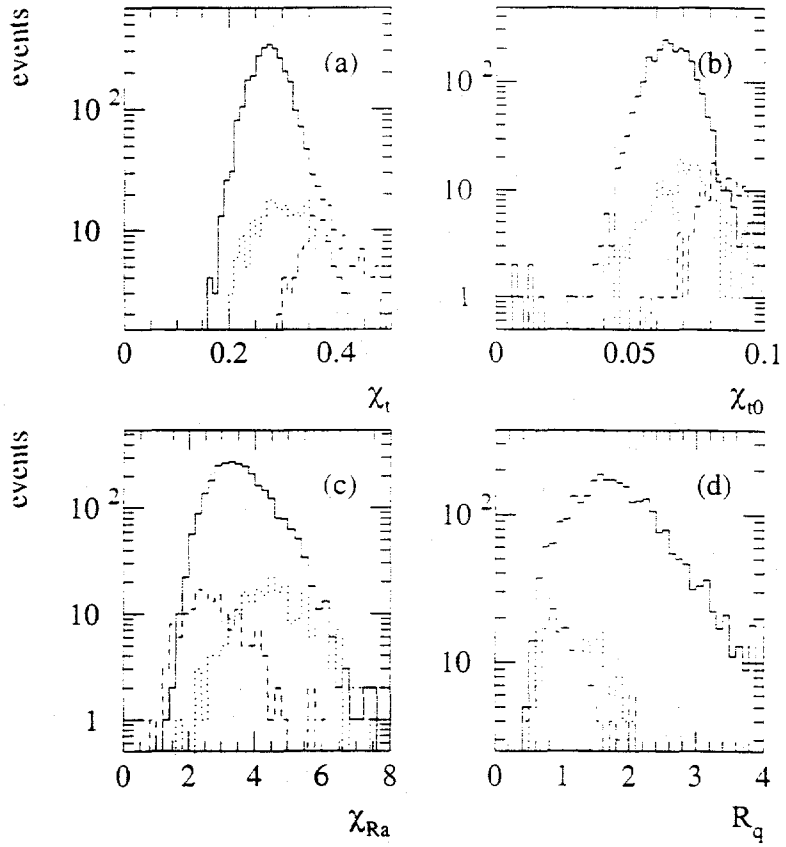

Figure 21. The electron reconstruction and PID efficiency as a function of visible charge.

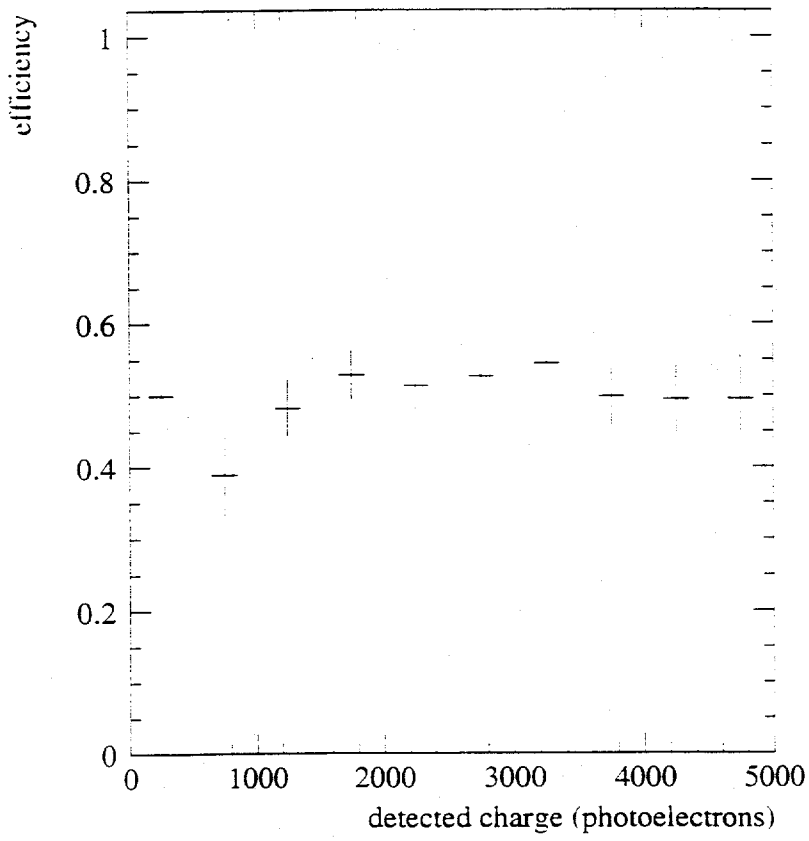

Figure 22. The (a) π^0 efficiency and (b) π^0/e^- efficiency ratio as a function of visible charge.

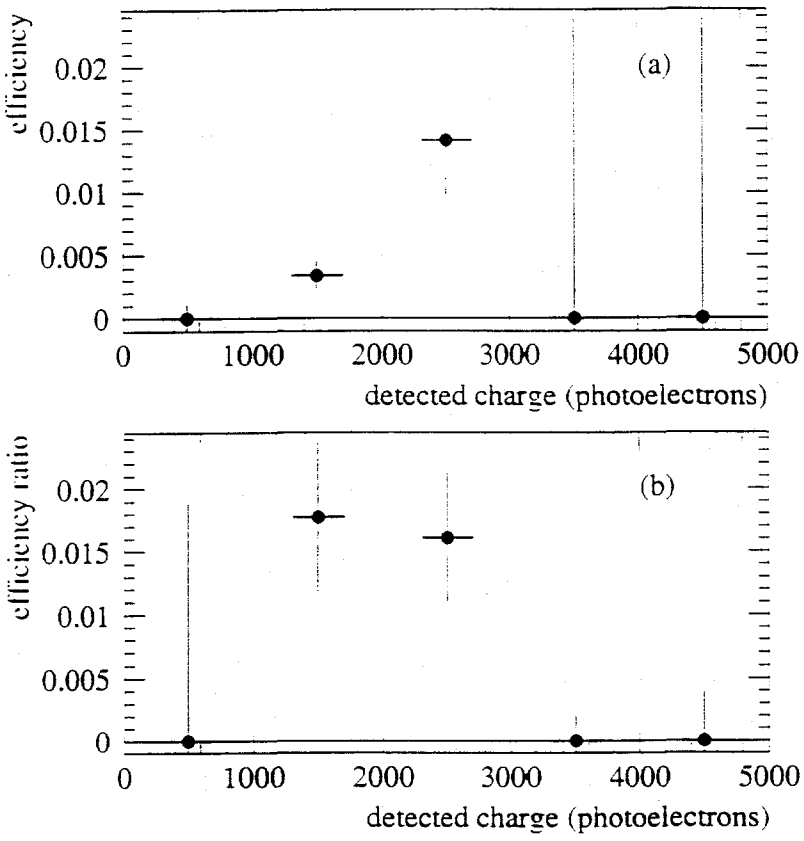

Figure 23. The cosine of the angle distribution between the two fitted Cerenkov rings for π^0 decays (dashed curve) and electrons (solid curve).